Polym. Bull. (2012) 68:1765–1776
DOI 10.1007/s00289-012-0702-5

ORIGINAL PAPER

Novel hydroxyapatite/tussah silk fibroin/chitosan bone-like nanocomposites

Jianxin He · Dongwei Wang · Shizhong Cui

Received: 21 January 2011 / Revised: 28 December 2011 / Accepted: 2 January 2012 /

Abstract The nanocomposite particles of hydroxyapatite–tussah silk fibroin (HA–TSF) and HA–chitosan (HA–CS) were developed by biomimetic synthesis using $Ca(NO_3)_2$ and Na_3PO_4 as the precursors of inorganic phase in the presence of TSF and CS. Both nanocomposite particles were carbonate-substituted HA with low crystallinity. TSF and CS induced preferential alignment of HA crystallites along the direction of *c*-axis, and the induction effect of TSF was more than of CS. HA–TSF and HA–CS nanocomposite particles were found to be needle-like in the shape with a typical size of 100–200 nm in length and about 20 nm in width, and 115–250 nm in length and about 25 nm in width, respectively, as the result of the preferential arrangement of HA crystallites along *c*-axis intensified by TSF and CS. Based on both nanocomposite particles, the bone-like nanocomposites of HA–TSF/CS and HA–CS/TSF with the same compositions were prepared by isostatic pressing using CS and TSF concentrated solutions as adhesive composition, respectively. However, the two bone-like nanocomposites exhibited significantly different mechanical properties. The compressive strength, compressive modulus, and bending strength of HA–TSF/CS composite were significantly higher than of HA–CS/TSF composite. The fracture mechanism of both composites was analyzed by SEM observation. The study result indicates that HA–TSF/CS nanocomposite is an ideal candidate for bone substitute materials.

Keywords Hydroxyapatite · Tussah silk fibroin · Chitosan · Nanocomposite

---

J. He (✉) · D. Wang · S. Cui
College of Textiles, Zhongyuan University of Technology, 41 Zhongyuan Road, P.O. Box 110,
Zhengzhou 450007, Henan, People's Republic of China
e-mail: hejianxin771117@163.com

Introduction

Natural bone is an inorganic–organic nanocomposite material comprising about 70 wt% of mineral phase, primarily hydroxyapatite (HA), and 30 wt% of organic matrix, primarily collagen fibrils [1, 2]. HA nanocrystals embedded orderly in collagen fibrils, and the distinctive harmony and the highly ordered assembly at the molecular level between the mineral phase and the organic matrix endow natural bone with homogenous porous microstructure and sufficient mechanical toughness and flexibility [3, 4]. However, exploiting bone-like composite material with microstructure and mechanical properties comparable to natural bone poses a significant challenge in tissue engineering. Growing efforts have been devoted to the fabrication of HA-based composites combined with bioactive polymers or proteins including collagen [1, 5], gelatin [6, 7], poly(lactic acid) [8], chitosan (CS) [9], silk fibroin [10, 11], chondroitin sulfate [12, 13], etc. The involvement of bioactive polymers or proteins can considerably improve the deficiency of HA ceramics such as intrinsic brittleness, poor formability, and migration of HA particles from the implanted sites.

Collagen is the major component of the organic matrix in natural bone. Kikuchi and co-workers [5] prepared a self-assembly HA/collagen nanocomposite by co-precipitation method, and found that the composite had a self-assembly structure similar to natural bone and showed good cell adhesion and proliferation for human osteoblast. However, a major concern for HA/collagen composite is the high cost of collagen, which limits its clinical application in healing bone defect.

Silk fibroin is another structural protein, having simple extraction process and sufficient source in contrast with collagen. Silk fibroins including mulberry silk (i.e., *Bombyx mori* silk) and wild silk are regarded as ideal material for biomedical application because of their good biocompatibility, biodegradability, non-cytotoxicity, and minimal inflammatory reaction. Wang et al. [10] and Cui and co-workers [14] prepared HA/*B. mori* silk fibroin composite, and found that the silk fibroin could induce the oriented growth of HA crystals and the introduction of silk fibroin intensified the micro-hardness of HA ceramic, however, HA/*B. mori* silk fibroin can not meet the requirement of bone substitution because of its insufficient formability and flexibility.

Tussah silk is one of the wild silks, and its chemical structure, molecular conformation, and physical properties have been extensively studied. In contrast to *B. mori* silk, its amino acid composition is characterized by more Ala, Asp, and Arg contents and less Gly [15]. Moreover, tussah silk contains the tripeptide sequence Arg-Gly-Asp (RGD) [16]. The RGD sequence in silk fibroins acts as a biological recognition signal and consequently promotes cell adhesion onto the fibroins [17], which also makes tussah silk fibroin (TSF) suitable for biomedical application.

CS, a natural polysaccharide containing active amino and hydroxyl groups, has excellent biocompatibility, biodegradability, and anti-infectivity. The brittleness of HA ceramics can be alleviated by the addition of CS due to its good plasticity and adhesivity. The study of Yamaguchi et al. [9] indicated that HA–CS composite was mechanically flexible and could mold into any desired shape.

This article employed TSF and CS as the organic matrix of HA particles to prepare novel HA/TSF/CS nanocomposite with good osteoconductivity, higher mechanical strength, and sufficient flexibility. HA–TSF and HA–CS nanocomposite particles were first obtained by coprecipitation method and the regulation effect of both organic matrixes to the crystallographic properties of HA were evaluated. Based on the two nanocomposite particles, both bone-like nanocomposites of HA–TSF/CS and HA–CS/TSF with the same compositions were prepared by isostatic pressing using CS and TSF concentrated solutions as adhesive composition, respectively. The differences between the two composites in mechanical properties and fracture mechanism were studied.

Experimental

Materials

Antheraea pernyi cocoon came from Henan province. CS with deacetylation degree of 90% and viscosity of 200 mPa s was supplied by Shanghai Chemical Reagent Co. Ltd., China. All chemicals employed were of analytical grades and purchased from commercial sources in China.

Preparation of regenerated TSF solution

To remove the sericin, *A. pernyi* cocoon was degummed using 0.5% Na_2CO_3 solution at 100 °C for three times. Degummed tussah fiber was dissolved in 9 M aqueous lithium thiocyanate solution at a liquor ratio of 10:1 by stirring at 55 °C for 1 h. Then the TSF aqueous solution was filtered to remove undissolved part, and then dialyzed for 3 days in deionized water to obtain regenerated TSF solution with a concentration of 0.5%.

Preparation of HA–TSF and HA–CS nanocomposite particles

Feed weight ratio of the inorganic component to organic component was set to 85/15. CS was dissolved in 2.0 wt% acetic acid aqueous solution to obtain 0.5 wt% CS solution. 5.608 g CaO was dissolved in 70 mL deionized water to obtain saturated $Ca(OH)_2$ suspension. The $Ca(OH)_2$ suspension and 85 wt% H_3PO_4 aqueous solution were slowly dropped into 354.35 g of 0.5 wt% TSF or CS solution at continuous stirring according to a Ca/P molar ratio of 1.67. The reaction solution was stirred vigorously for 2 h at 60 °C and titrated with ammonia water in drops to maintain the pH at 8.0–9.0. The products was centrifuged and washed with deionized water alternately to harvest the precipitates. The precipitates were vacuum-dried at 50 °C for 24 h and subsequently ground using an agate mortar in order to obtain HA–TSF or HA–CS powders. The weight ratio of the inorganic component to organic component was determined to 86.4/13.6 in both particles using TG analysis, almost consistent with the theoretical yield weight ratio.

Meanwhile, pure HA without TSF and CS was prepared as control sample by the same procedure.

Preparation of HA–TSF/CS and HA–CS/TSF nanocomposites

HA–TSF nanocomposite particles and *p*-dichlorobenzene at the same weight ratio were fully mixed at ultrasonic vibration. Five wt% CS concentrated solution was then added, followed by a preforming in a column mold at 1.5 MPa pressure and an isostatic compaction at 250 MPa. The *p*-dichlorobenzene in the product was removed by 8 h sonic oscillation in ethanol and subsequently vacuum-dried at 80 °C to obtain HA–TSF/CS nanocomposite.

The contents of TSF and the adhesive of CS in HA–TSF/CS nanocomposite were desired to keep the same, thus the weight ratio of HA/TSF/CS in HA–TSF/CS nanocomposite was 76/12/12, which was approximate to the inorganic/organic weight ratio (75/25) of natural bone. Meanwhile, HA–CS/TSF nanocomposite was prepared based on HA–CS nanocomposite particles using *p*-dichlorobenzene as pore-forming agent and 5 wt% TSF concentrated solution as adhesive according to the same procedure. The relative contents of the components were consistent in both nanocomposites.

Characterization of the materials

The SEM images of samples were observed on a scanning electron microscope (Cold-Field Emission SEM S-4800, Hitachi) with an accelerating voltage of 1.0 kV.

X-ray diffractions of nanoparticles were record at a scanning speed of 0.02° s^{-1} with a Rigaku-D/Max-2550PC diffractometer using Ni-filtered Cu K_α radiation of wavelength 0.1542 nm. The operating voltage and current were 40 kV and 30 mA, respectively. The average size of crystallite was calculated from the Scherrer equation.

FTIR spectra of HA, HA–TSF, and HA–CS nanoparticles were recorded with a Nicolet Nexus 670 FTIR spectrometer, using the KBr disc technique (1.0 mg nanoparticle sample/300 mg KBr). One hundred scans were taken with a resolution of 2 cm^{-1}.

Thermogravimetric (TG) analysis was carried out on Perkin Elmer TGA TG analysis instrument. All the experiments were carried out with the same nitrogen flux. The heating-up speed was 10 °C min^{-1} and the degradation temperature was from 25 to 1,000 °C.

The compressive and bending properties of HA–TSF/CS and HA–CS/TSF composites were measured on an Instron 5582 tester. The samples with a size of $10 \times 10 \times 5$ mm^3 were used in compressive property test with a loading velocity of 2 mm min^{-1}. The samples with a size of $50 \times 40 \times 5$ mm^3 were used in bending property test with a span length of 15 mm and a loading velocity of 2 mm min^{-1}. The reported data of compressive and bending properties represent the average results of ten tests.

Results and discussion

Preparation and characterization of HA–TSF and HA–CS nanocomposite particles

X-ray diffraction patterns of HA, HA–TSF, and HA–CS nanocomposite particles are shown in Fig. 1. The three nanocomposites exhibit the peaks at the similar position, assigned only to monophase crystalline HA, since no diffraction peaks from other calcium phosphate phases are observed. This indicates that the addition of TSF and CS did not change the crystalline structure of HA. The X-ray diffraction patterns show a preferential growth of HA crystallites along *c*-axis in all three nanoparticles, since the intensity of (002) peak is obviously higher than that of (300) peak [18]. HA–TSF and HA–CS nanocomposite particles present the broader peaks with lower intensity than pure HA particle, suggesting that both HA composite particles modulated by the two biopolymers have small crystallite sizes and low crystallinity similar to natural bone minerals [3].

As shown in Table 1, the calculated results of crystallite sizes demonstrated a reduction of the two composite particles in the crystallite sizes both along *c*-axis (L_c) and along *a*-axis (L_a) as compared to pure HA particles. However, both TSF and CS has the effect of inducing HA crystallite to preferentially growth along

Fig. 1 X-ray diffraction patterns of (*a*) pure HA, (*b*) HA–TSF, and (*c*) HA–CS nanoparticles

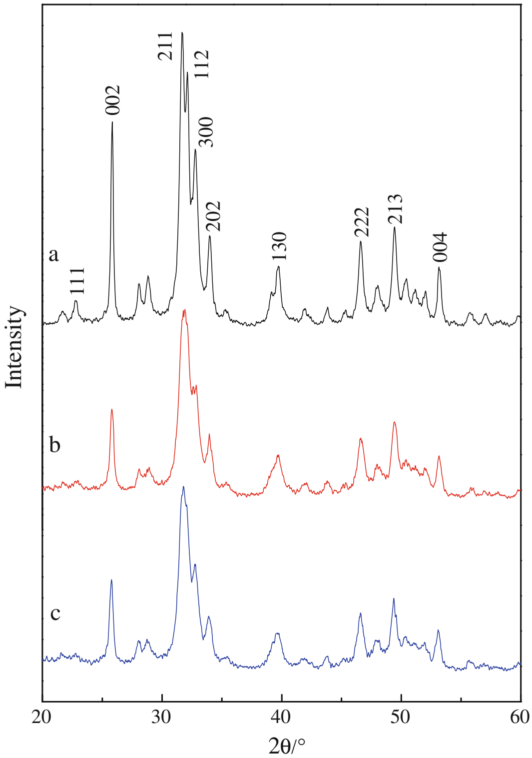

Table 1 Crystal sizes and crystallographic parameters of HA crystallites

Samples	L_c (002) (nm)	FWHM (°)	L_a (300) (nm)	FWHM (°)	a (nm)	c (nm)	L_c/L_a
HA	37.35	0.2205	15.32	0.5757	0.9437	0.6880	1.79
HA–TSF	27.48	0.2997	13.91	0.6340	0.9439	0.6901	2.60
HA–CS	26.35	0.3124	14.26	0.6186	0.9440	0.6888	2.32

c-axis through comparing the aspect ratio of L_c/L_a and the cell parameters of HA crystallites, and the induction action of TSF was more obvious than CS.

Figure 2 shows the FTIR spectra of TSF, HA–TSF, HA–CS, and HA nanocomposite particles, where the characteristic bands of HA are observed. The bands at 1092, 1035, 961 cm^{-1} correspond to different modes of PO_4^{3-} group in HA. The weak band at 875 cm^{-1} is due to the vibration of HPO_4^{2-} indicating of small amount of calcium-deficient apatite in the three products. The bands at 1,422 and 1,454 cm^{-1} can be distinguished by the CO_3^{2-} group, suggesting that the carbonate ion was incorporated into the HA crystallite due to the CO_2 from atmosphere during agitating [19]. Thus, the characteristic of these HA particles coincides with that in natural bone. The band at 1,636 cm^{-1} corresponds to the characteristic absorption of OH group of HA, which presents as a sharper peak at 1,641 cm^{-1} in HA–TSF nanocomposite particles, possibly ascribed to the overlap of the bands of OH group in HA and amide I in TSF. Pure TSF exhibits the amide I

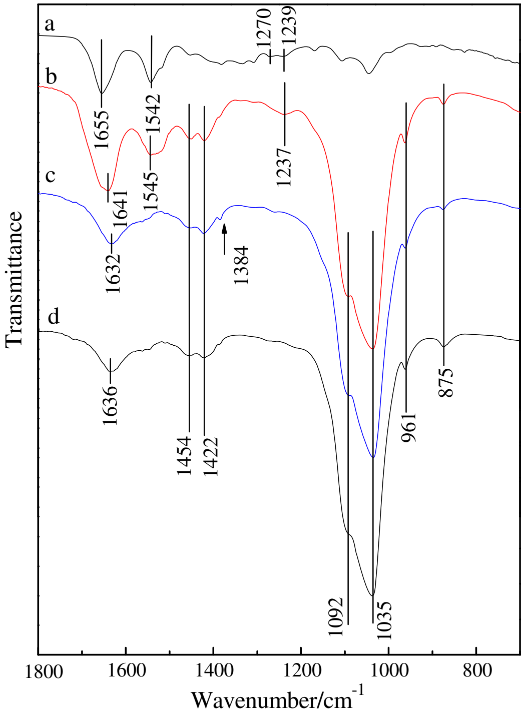

Fig. 2 FTIR spectra of (*a*) pure TSF, (*b*) HA–TSF, (*c*) HA–CS, and (*d*) pure HA nanoparticles

absorption at 1,655 cm^{-1}. In addition, there are the absorption bands at 1,545 and 1,237 cm^{-1} attributed to the amide II and amide III of TSF in HA–TSF particles, whereas pure TSF shows the amide II band at 1,542 cm^{-1} and the amide III bands at 1,270 and 1,239 cm^{-1} [20]. These differences suggest that there is distinguished chemical interaction between the HA crystal and TSF.

CS shows only a small absorption peak at 1,384 cm^{-1} assigned to the symmetric deformation vibration of CH_3 group in HA–CS composite particles. Other characteristic bands of CS such as amide I (C=O), amino ($-NH_2$), and CH deformation are not easily detected in composite particles. One possible reason is that these bands position at 1656, 1602, and 1425 cm^{-1}, which overlapped with the absorption bands of HA.

The morphology and size of HA, HA–TSF and HA–CS nanoparticles were investigated using FE-SEM (Fig. 3). Pure HA particles present the short rod shape with a size of 100–200 nm in length and about 45 nm in width. Pure HA nanoparticles are in relatively well-dispersed state, whereas the severe agglomeration in both composite particles. HA–TSF and HA–CS nanocomposite particles are envisioned as needle-like in the shape with a typical size of 100–200 nm in length and about 20 nm in width, and 115–250 nm in length and about 25 nm in width, respectively. Both composite nanoparticles are all the result of the agglomeration due to the organic polymers existing between the HA crystallites. The introduction of TSF and CS enhanced the aggregation of HA crystallite and promoted the arrangement of HA crystallite along *c*-axis [18].

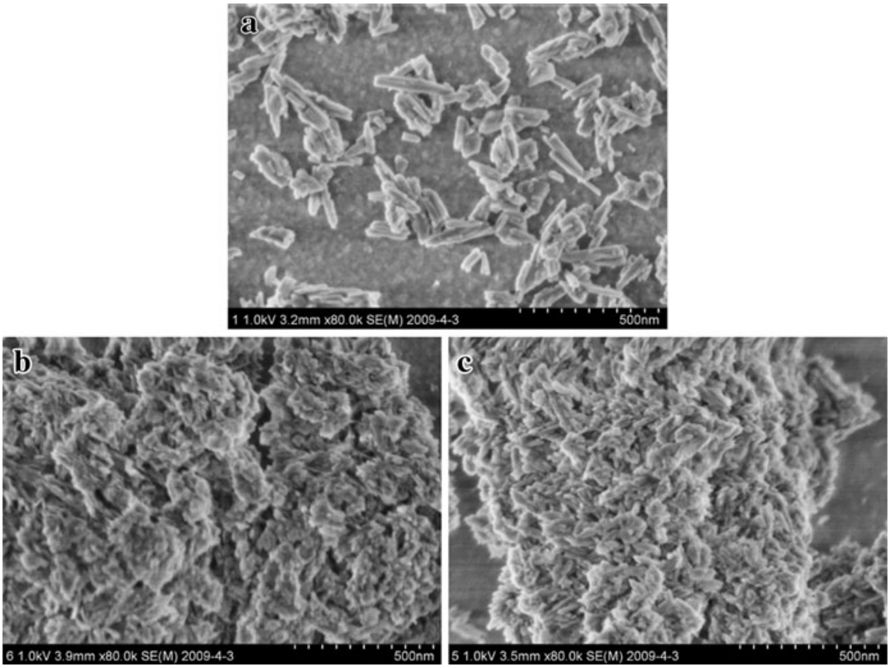

Fig. 3 SEM images of **a** pure HA, **b** HA–TSF, and **c** HA–CS nanoparticles (×80,000)

TG curves of pure HA, HA–TSF, and HA–CS nanoparticles are shown in Fig. 4. TG curve of pure HA particles display a continuous weight loss of 7.5% from 50 °C onward until 600 °C, and a notable weight loss in the range of 50–150 °C, which can be ascribed to water evaporation. There is no weight loss occurred above 600 °C, suggesting that pure HA is thermally stable at high temperature.

The weight of both nanocomposite particles decreases rapidly with increasing temperature and the initial weight loss in the range of 25–150 °C is assigned to water evaporation. The thermal decomposition of the organic component in HA–TSF composite particles occurred mostly in the range of 240–440 °C with a temperature at maximum decomposition rate of 353 °C, and the organic component are decomposed completely at 710 °C. The thermal stability of HA–CS nanocomposite particles is less than that of HA–TSF, and the decomposition of organic component mostly occurred in the range of 220–400 °C with a temperature at maximum decomposition rate of 312 °C. However, there is no change in the weight of HA–CS composite particles up to the temperature above 890 °C, indicating that the organic component in the composite particles decomposed completely at a high temperature of 890 °C. The organic/inorganic weight ratios in both nanocomposite particles except from water content are almost identical, and determined to be 13.6/86.4, almost similar to the designed theoretical weight ratio (15/85). Thermal analysis indicates that TSF and CS molecules have been well embedded into the composite particles with HA.

Mechanical properties of HA–TSF/CS and HA–CS/TSF nanocomposites

The compressive stress–strain curves of HA–TSF/CS and HA–CS/TSF nanocomposites are shown in Fig. 5. The initial parts in the tensile curves of both nanocomposites show a linear region with higher initial modulus. As compared to HA–CS/TSF, HA–TSF/CS nanocomposite exhibits a higher initial modulus. Since ethanol treated TSF is the silk II structure [21], the rigidity of HA–TSF nanoparticles is higher than of HA–CS, which is the principal in both composites.

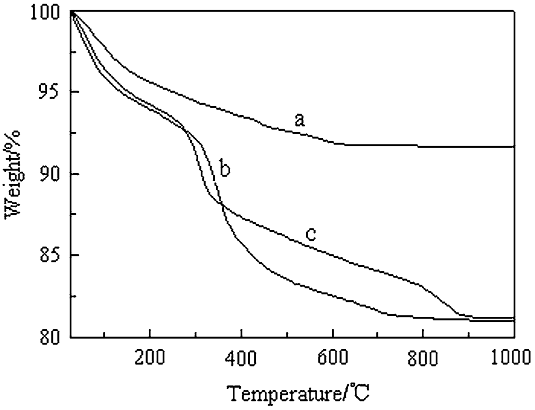

Fig. 4 TG curves of (*a*) pure HA, (*b*) HA–TSF, and (*c*) HA–CS nanoparticles

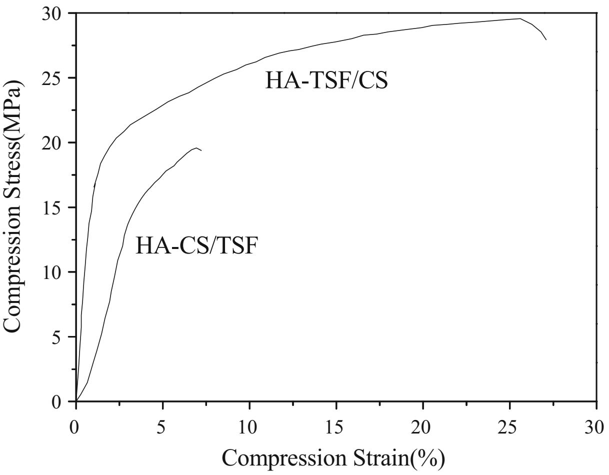

Fig. 5 Compressive stress–strain curves of HA–TSF/CS and HA–CS/TSF nanocomposites

A yield point is also observed after the initial linear portion of the stress–strain curves followed by a gradual reduction region in modules. In this region, there is a greater compressive strain in HA–TSF/CS nanocomposite, while HA–CS/TSF fractured immediately after yielding. This can be explained by the fact that the nanoparticles for the former were adhered by the flexible CS, whereas adhered by the crystallized TSF for the latter.

Table 2 shows the mechanical properties of HA–TSF/CS and HA–CS/TSF nanocomposites. Although the composition, density and porosity of both nanocomposites are similar, there are significant differences in their mechanical properties. The compressive strength, compressive modulus, and bending strength of HA–TSF/CS nanocomposite were 28.9 MPa, 15 GPa, and 17.8 Mpa, respectively, which were significantly higher than of HA–CS/TSF.

The morphology of the two nanocomposites at fracture section was observed by SEM in order to study the fracture mechanism further (Fig. 6). Both nanocomposites are rough and uneven in fracture section, presenting a three-dimensional network formed by the crosslinking of biopolymers with nanoparticles distributed irregularly on them. Many interconnected pores distributed over HA–TSF/CS and HA–CS/TSF nanocomposite with more uniform pore size in the former. The

Table 2 Mechanical properties of HA–TSF/CS and HA–CS/TSF nanocomposites

Samples	Compressive strength (MPa)	Compressive yield strength (MPa)	Compressive modulus (GPa)	Bending strength (MPa)	Porosity (%)	Density (g cm^{-3})
HA–TSF/CS	28.91	20.65	15	17.85	46	0.72
HA–CS/TSF	19.45	15.57	5	5.42	41	0.67

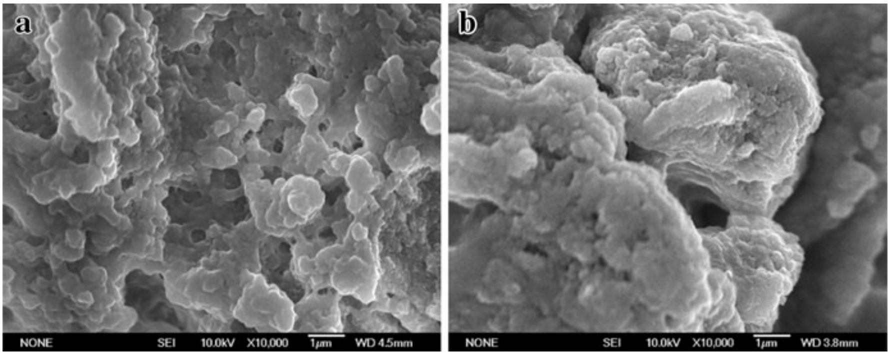

Fig. 6 SEM images of **a** HA–CS/TSF and **b** HA–TSF/CS nanocomposites (×10,000)

Fig. 7 Fracture schematics of **a** HA–CS/TSF and **b** HA–TSF/CS nanocomposites

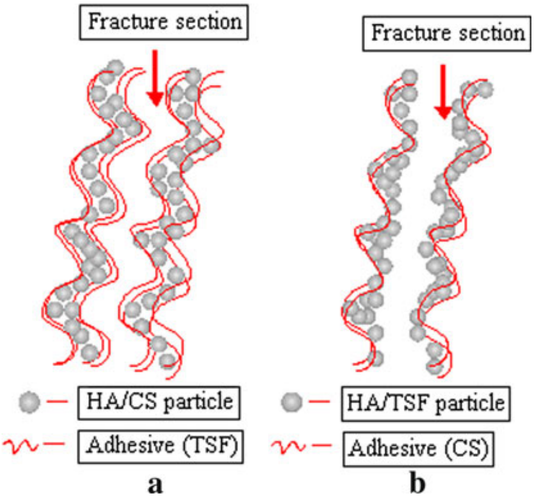

nanoparticles in the fracture section of HA–CS/TSF nanocomposite exhibit a smooth surface, thought to be due to the adhesion of TSF molecules on the surface of nanoparticles. It indicates that the rupture of HA–CS/TSF nanocomposite occurred in the interior of adhesive phase (i.e., TSF) mostly due to the TSF phase is rigid and relatively brittle, and its fracture schematic is shown in Fig. 7a.

However, HA–TSF/CS nanocomposite shows another morphology at fracture section (Fig. 6b), and many rough nanoparticles exposed on its fracture section. A possible explanation for the finding is proposed in the Fig. 7b. Owing to stronger intermolecular interaction of adhesive phase itself (i.e., CS), the fracture of the nanocomposite did not occur within the adhesive phase, but between the nanoparticles that were not blend fully with the adhesive. Of course, there is another possibility that HA–TSF/CS is more homogeneous (HA–TSF nanoparticles disperse in CS better) than HA–CS/TSF, therefore, it shows much better mechanical properties and the nanoparticles appear on the fracture surface. Therefore, the organic component of nanocomposites affects their mechanical properties significantly. The crystallized organic phase in nanocomposite particles can intensity the mechanical properties of composite while the rigid organic phase in adhesive decreases the mechanical properties.

Conclusions

The two nanocomposite particles of HA–TSF and HA–CS were prepared by a coprecipitation method with TSF and CS serving as the organic phase, respectively. TSF and CS molecules can be used as the template to induce the preferential growth of HA crystallite and promote the arrangement of HA crystallite along *c*-axis, resulted in the formation of needle-like morphology. Both nanocomposite particles were carbonate-substituted HA with low crystallinity similar to natural bone. Although HA–TSF/CS and HA–CS/TSF nanocomposites have the similar composition, density and porosity, the mechanical properties of HA–TSF/CS were significantly greater than of HA–CS/TSF. The rupture of HA–CS/TSF nanocomposite occurred in the interior of adhesive, whereas the rupture of HA–TSF/CS occurred between the nanoparticles without blending fully with the adhesive. HA–TSF/CS nanocomposites can be used as an ideal candidate for bone substitute materials.

Acknowledgments This research was financially supported by the Programme of Introducing Talents of Discipline to Universities, B07024, China, and we also acknowledged the support from China Postdoctoral Science Foundation funded project (20080430079, 200902194).

References

1. Kikuchi M, Itoh S, Ichinose S, Shinomiya K, Tanaka J (2001) Self-organization mechanism in a bone-like hydroxyapatite/collagen nanocomposite synthesized in vitro and its biological reaction in vivo. Biomaterials 22:1705–1711
2. Du C, Cui FZ, Zhang W, Feng QL, Zhu XD, Groot KD (2000) Formation of calcium phosphate/collagen composites through mineralization of collagen matrix. J Biomed Mater Res 50:518–527
3. Rho JY, Kuhn-Spearing L, Zioupos P (1998) Mechanical properties and the hierarchical structure of bone. Med Eng Phys 20:92–102
4. Fratzl P, Weinkamer R (2007) Nature's hierarchical materials. Prog Mater Sci 52:1263–1334
5. Chang MC, Ikoma T, Kikuchi M, Tanaka J (2001) Preparation of a porous hydroxyapatite/collagen nanocomposite using glutaraldehyde as a crosslinkage agent. J Mater Sci Lett 20:1199–1201
6. Yin YJ, Zhao F, Song XF, Yao KD, Lu WW, Leong JC (2000) Preparation and characterization of hydroxyapatite/chitosan–gelatin network composite. J Appl Polym Sci 77:2929–2938
7. Bigi A, Boanini E, Panzavolta S, Roveri N, Rubin K (2002) Bonelike apatite growth on hydroxyapatite–gelatin sponges from simulated body fluid. J Biomed Mater Res 59:709–714
8. Ma PX, Zhang RY, Xiao GZ (2007) Enginering new bone tissue in vitro on highly porous poly(*a*-hydroxyl acids)/hydroxyapatite composite scaffolds. J Biomed Mater Res 54:284–293
9. Yamaguchi I, Tokuchi K, Fukuzaki H (2007) Preparation and microstructure analysis of chitosan/hydroxyapatite nanocomposites. J Biomed Mater Res 55:20–27
10. Wang L, Nemoto R, Senna M (2004) Changes in microstructure and physico-chemical properties of hydroxyapatite–silk fibroin nanocomposite with varying silk fibroin content. J Eur Ceram Soc 24:2707–2715
11. Nemoto R, Wang L, Ikoma T, Tanaka J, Senna M (2004) Preferential alignment of hydroxyapatite crystallites in nanocomposites with chemically disintegrated silk fibroin. J Nanopart Res 6:259–265

12. Rhee SH, Tanaka J (2002) Self-assembly phenomenon of hydroxyapatite nanocrystals on chondroitin sulfate. J Mater Sci Mater Med 13:597–600
13. Rhee SH, Tanaka J (2000) Effect of chondroitin sulfate on the crystal growth of hydroxyapatite. J Am Ceram Soc 83:2100–2102
14. Sun XD, Zhou YL, Ren JY, Cui FZ, Li HD (2007) Effect of pH on the fibroin regulated mineralization of calcium phosphate. Curr Appl Phys 7:75–79
15. He JX, Wang Y, Cui SZ, Gao YY, Wang SY (2010) Structure and miscibility of tussah silk fibroin/carboxymethyl chitosan blend films. Iran Polym J19:625–633
16. Minoura N, Aiba SI, Higuchi M (1995) Attachment and growth of fibroblast cells on silk fibroin. Biochem Biophys Res Commun 8:511–516
17. Pierschbacher MD, Ruoslahti E (1984) Cell attachment activity of fibronectin can be duplicated by small synthetic fragments of the molecule. Nature 309:30–33
18. Cai Y, Jin J, Mei D, Xia N, Yao J (2009) Effect of silk sericin on assembly of hydroxyapatite nanocrystals into enamel prism-like structure. J Mater Chem 19:5751–5758
19. Chang MC, Tanaka J (2002) FT-IR study for hydroxyapatite/collagen nanocomposite cross-linked by glutaraldehyde. Biomaterials 23:4811–4818
20. Fredd G, Monti P, Nagura M, Gotoh Y, Tsukada M (1997) Structure and molecular conformation of tussah silk fibroin films: effect of heat treatment. J Polym Sci B 35:841–847
21. Nakazawa Y, Asakura T (2002) High-resolution 13C CP/MAS NMR study on structure and structural transition of *Antheraea pernyi* silk fibroin containing poly(L-alanine) and gly-rich regions. Macromolecules 35:2393–2400